OXFORD

Cerebral Cortex, February 2021;31: 1032–1045

doi: 10.1093/cercor/bhaa272
Advance Access Publication Date: 30 September 2020
Original Article

ORIGINAL ARTICLE

Microstructure of Human Corpus Callosum across the Lifespan: Regional Variations in Axon Caliber, Density, and Myelin Content

Jonathan D. Lynn[1,2,†], Chaitali Anand[1,2,†], Muzamil Arshad[1], Roya Homayouni[2,3], David R. Rosenberg[1], Noa Ofen[2,3,4], Naftali Raz[2,3,5] and Jeffrey A. Stanley[1]

[1]Department of Psychiatry and Behavioral Neurosciences, Wayne State University School of Medicine, Detroit MI 48201, USA, [2]Institute of Gerontology, Wayne State University, Detroit MI 48202, USA, [3]Department of Psychology, Wayne State University, Detroit MI 48201, USA, [4]Lifespan Cognitive Neuroscience, Merrill Palmer Skillman Institute, Wayne State University, Detroit MI 14195, USA and [5]Center for Lifespan Psychology, Max Planck Institute for Human Development, Berlin 14195, Germany

Address correspondence to Jeffrey A. Stanley, PhD, Brain Imaging Research Division. 3901 Chrysler Dr Detroit, MI 48201, USA. Email: jeffrey.stanley@wayne.edu; Naftali Raz, PhD, Institute of Gerontology. 87 East Ferry St. Detroit, MI 48202 USA. Email: nraz@wayne.edu.

[†]These authors have contributed equally to this work.

Abstract

The myeloarchitecture of the corpus callosum (CC) is characterized as a mosaic of distinct differences in fiber density of small- and large-diameter axons along the anterior–posterior axis; however, regional and age differences across the lifespan are not fully understood. Using multiecho T_2 magnetic resonance imaging combined with multi-T_2 fitting, the myelin water fraction (MWF) and geometric-mean of the intra-/extracellular water T_2 ($geomT_{2IEW}$) in 395 individuals (7–85 years; 41% males) were examined. The approach was validated where regional patterns along the CC closely resembled the histology; MWF matched mean axon diameter and $geomT_{2IEW}$ mirrored the density of large-caliber axons. Across the lifespan, MWF exhibited a quadratic association with age in all 10 CC regions with evidence of a positive linear MWF-age relationship among younger participants and minimal age differences in the remainder of the lifespan. Regarding $geomT_{2IEW}$, a significant linear age × region interaction reflected positive linear age dependence mostly prominent in the regions with the highest density of small-caliber fibers—genu and splenium. In all, these two indicators characterize distinct attributes that are consistent with histology, which is a first. In addition, these results conform to rapid developmental progression of CC myelination leveling in middle age as well as age-related degradation of axon sheaths in older adults.

Key words: aging, corpus callosum, development, myelin, T_2 relaxation

Introduction

The human cerebral cortex exhibits substantial regional differences in cytoarchitecture (Brodmann 1908) and shows marked heterochronicity of development and aging (Raz and Rodrigue 2006). In this context, the corpus callosum (CC) that connects homologous cortical regions across the hemispheres represents an optimal and compact model system for studying regional brain differences and differential effects of age on them across the lifespan.

The CC is the largest white matter commissure of the human brain with fibers forming distinct regional groupings that approximate the topographic representation of cortical regions which they connect (Pandya et al. 1971; Seltzer and Pandya 1983; Barbas and Pandya 1984; de Lacoste et al. 1985; LaMantia and

Rakic 1990a; Aboitiz et al. 1992). Structural heterogeneity of the CC corresponds to its functional diversity, as the regional differences in axon diameter, and density as well as myelin sheath thickness corresponds to the functional particularities of transmission requirements between the connected cortical areas (LaMantia and Rakic 1990b; Aboitiz et al. 1992). In addition, the CC undergoes dramatic age-related differences attributable to the maturational processes and effects of experience. Early in postnatal development a substantial pruning of callosal axons coincides with the early phases of developmental myelination (Berbel and Innocenti 1988; LaMantia and Rakic 1990a). Postmortem studies demonstrate that the process of myelination, while accelerated during childhood and adolescence, continues well into the middle age. In addition, the myelin-age relationship varies vastly among cortical regions suggesting significant heterochronicity of myelination (Flechsig 1901; Kaes 1907; Yakovlev and Lecours 1967). Myelin content, however, is not the only white matter property that varies across the lifespan. Maturation and aging are also accompanied by profound changes in the caliber, density of myelinated and unmyelinated axons and the distance among them (Lintl and Braak 1983; Tang et al. 1997; Peters and Sethares 2002; Marner et al. 2003; Hou and Pakkenberg 2012), with structural degradation of myelin sheaths appearing in advanced age (Peters and Sethares 2002), which are not fully understood.

Postmortem studies have the advantage of providing detailed information on the CC microstructure with exquisite precision and single-cell resolution, but suffer from providing within subject changes over time or associations with changes in behavior and cognition. Magnetic resonance imaging (MRI) has the ability to overcome these limitations, albeit at the expense of spatial resolution. For example, in vivo structural MRI studies have revealed significant life-span differences in gross structural properties of white matter such as regional volume (Raz et al. 1997; Westlye et al. 2010) and water diffusion characteristics derived from diffusion tensor imaging (DTI) (Salat, Tuch, Greve et al. 2005; Hasan et al. 2009; Michielse et al. 2010; Lebel et al. 2012; Bennett and Madden 2014; Mårtensson et al. 2018). However, DTI-derived indices, while sensitive to microstructural alterations, are difficult to interpret due to multiple factors that can alter water diffusion, including fiber caliber, density, size of the intra- and extracellular space, and the presence of crossing fibers (Jones et al. 2013).

Multiecho T_2 imaging (ME-T_2) combined with multiple T_2 component fitting is an MRI technique with greater ability in characterizing distinct attributes of the myelin microstructure and provides robust, reliable, and stable indices of the white matter microstructure (Arshad et al. 2017; Anand et al. 2019). The approach is based on the quantification of multiple T_2 relaxation components reflecting unique physical environments of water mobility in the white matter microstructural components (Carr and Purcell 1954; Meiboom and Gill 1958; MacKay et al. 1994; Whittall et al. 1997). That is, T_2 relaxation of water is directly related to water mobility and therefore allows discerning the signal of water trapped between myelin sheaths from water in the extracellular space of large, sparsely packed axons with greater interaxon distances or small, densely packed axons. The shortest T_2 component of approximately 10–15 ms at 3 Tesla (Curnes et al. 1988; Menon et al. 1992) is attributed to immobile water molecules trapped between the myelin sheaths. Its signal amplitude relative to the total water signal reflects myelin content and is termed the myelin water fraction (MWF). MWF has been extensively validated (Webb et al. 2003; Laule et al. 2006; Laule et al. 2008; McCreary et al. 2009) and shows nonlinear age-related differences across major white matter tracts (Arshad et al. 2016) that mirror those observed in classic postmortem studies of the cerebral cortex (Kaes 1907). However, the association of MWF to a specific attribute of the myelin microstructure is unknown (e.g., does myelin content relate to the mean axon size, density, or interaxon distance). In contrast, the intermediate T_2 component is attributed to relatively mobile water molecules in the intra- and extracellular space. Its geometric mean, $\text{geom}T_{2\text{IEW}}$, ranges between 55 and 80 ms at 3 Tesla and increases with axon size and interaxon distance (Whittall et al. 1997; Dula et al. 2010; Does 2018). Further, there is evidence of age-related differences in $\text{geom}T_{2\text{IEW}}$ values across white matter tracts (Billiet et al. 2015), and it may, therefore, reflect age-related processes of myelin sheath degradation/disruption that was reported in humans and other primate species (Peters and Sethares 2002). Again, however, in addition to evidence of age-related differences, the association of $\text{geom}T_{2\text{IEW}}$ to a specific attribute of the myelin microstructure is also unknown.

To date, however, unlike volumetric and DTI investigations, ME-T_2 studies of MWF have been limited to healthy adults (Billiet et al. 2015; Arshad et al. 2016) and persons with degenerative diseases of the white matter (Laule et al. 2006; Laule et al. 2008; Borich et al. 2013; Vargas et al. 2015), with virtually no studies in the literature characterizing the myelin microstructure of the CC across the full lifespan of healthy individuals. Moreover, because of the well-characterized details on the mosaic of regional differences in fiber properties across the CC from histological investigations, as noted above, this provides a grounded reference for associating the myelin imaging metrics, MWF, and $\text{geom}T_{2\text{IEW}}$, to specific attributes of the myelin microstructure. Addressing these lacunae in the current knowledge was the main motivation for the study reported here.

The aim of our investigation was 2-fold. First, we examined, in vivo, the differences among the CC regions that are histologically characterized by distinct patterns of axonal caliber, density, and myelination (Aboitiz et al. 1992). The enhanced sensitivity of ME-T_2 to tissue microstructure, relative to other imaging modalities, makes it an optimal tool for investigating regional patterns of microstructure that have, thus far, only been characterized in postmortem tissue. Second, we used the CC as a model system of white matter development and aging to assess lifespan differences in myelin content indexed by MWF, and axon caliber and density for which $\text{geom}T_{2\text{IEW}}$ serves as a proxy measure.

Materials and Methods

Participants

The sample consisted of 395 healthy individuals (161 males), between the ages of 7 and 85 years [M = 30.9 years, standard deviation (SD) = 22.0 years], recruited from the Detroit metropolitan area for three separate longitudinal studies. A portion of the young adults, and all of the middle-aged and older adults participated in a longitudinal study of aging (for sample description see ([Bender and Raz 2015)]. All children, adolescents, and another group of young adults were recruited either as control subjects for a study of obsessive–compulsive disorder [OCD, (Friedman et al. 2017)] or as healthy, typically developing children and adolescents for a study of brain and cognitive development (Yu et al. 2018).

All participants were screened via a phone interview, a written questionnaire, or both regarding medical history, and disqualified from participation if they had a history of neurological/psychiatric illness or head trauma. Exclusion criteria specific to the aging study included a history of cancer, cardiovascular disease (excluding medically treated hypertension), cerebrovascular disease, metabolic or endocrine disorders and the use of antiepileptic, anxiolytic, or antidepressant medication. Participants of the aging study were also disqualified if they received a score below 26 on the mini-mental state examination (Folstein et al. 1975) or above 15 on the geriatric depression questionnaire (Radloff 1977). Recruits for the OCD study were accepted only if they were of European Caucasian descent, had never been diagnosed with any psychiatric illness or Mendelian genetic disorder, and scored ≥80 on the Wechsler Abbreviated Scale of Intelligence, Version II. Unlike the rest of the studies, participants of the OCD study were not exclusively right-handed. Consent obtained from all participants followed the procedures of the Wayne State University institutional review board. Parental consent was required from participants under the age of 18 years.

MRI Acquisition and Processing

All imaging was performed on the same 3 Tesla MRI system (Siemens MAGNETOM Verio™) with a 12-channel radiofrequency coil. Though the imaging data came from several ongoing investigations, the ME-T_2 acquisition protocol was identical in all studies. The structural T_1-weighted imaging protocol was identical for the majority of the data except for 25 subjects, which differed slightly, as noted below.

ME-T_2 images were acquired in the axial plane with a 3D-gradient and spin-echo (GRASE) sequence provided by Dr Jongho Lee (Seoul National University), which was based on a previously developed sequence (Prasloski et al. 2012). Acquisition parameters for the 3D-GRASE sequence were as follows: repetition time (TR) = 1110 ms, number of echoes = 32, first echo time (TE) = 11 ms, interecho spacing = 11 ms, field of view (FOV) = 165 × 220 mm^2, matrix size = 144 × 192, slice thickness = 5 mm, number of axial slices = 24, and in-plane resolution = 1.15 × 1.15 mm^2. The acquisition time for the 3D-GRASE sequence was ~17 min. We do acknowledge that acquiring the ME-T_2 images in the axial plane was not optimal for assessing the CC, which has larger dimensions along the rostral–caudal rather than ventral–dorsal axis, because our protocol was designed for covering a broad range of white-matter tracts in the brain. For 370 of the 395 participants a T_1-weighted magnetization-prepared rapid gradient-echo (MPRAGE) scan was collected using the following parameters: echo time (TE) = 4.38 ms, TR = 1600 ms, inversion time (TI) = 800 ms, FOV = 256 × 256 mm^2, voxel size = 0.67 × 0.67 × 1.34 mm^3, matrix size = 384 × 384, flip angle = 8°, and GRAPPA factor = 2. The total acquisition time for the MPRAGE sequence was 5:41 min. For the remaining 25 participants, a T_1-weighted MP2RAGE (Marques et al. 2010) scan was collected with the following parameter: TE = 3.52 ms, TR = 6250 ms, TI = 800/2200 ms, FOV = 256× 256 mm^2, matrix size = 256 × 256, isometric 1 mm^3 voxel, and flip angle = 7/5.

Segmentation of the CC

The CC was divided into 10 regions of interest (ROIs), following the scheme described by Björnholm et al. (2017) and modified by Anand et al. (2019). The CC regions were demarcated on the midsagittal slice in the Montreal Neurological Institute (MNI152) standard space using the FMRIB Software Library's FSL view (Jenkinson et al. 2012). The CC regions defined in the MNI space were extended laterally by 7 mm from midline into each hemisphere to attain a more comprehensive coverage of the CC as illustrated in Figure 1. The lateral extension was selected to correspond to a typical location of lateral longitudinal stria on the CC dissections (Di Ieva et al. 2015), thus capturing the bulk of callosal tissue while reducing the likelihood of including extracallosal extensions—the forceps minor and major.

In the process of ROI demarcation, the CC was first divided into three equal segments along a straight line between its anterior and posterior-most tips. These three segments account for the genu, body, and isthmus + splenium of the CC from anterior to posterior. The genu and body were subdivided further into three equal segments based on their respective length (GENU1–3 and BODY1–3). The posterior third was separated into the isthmus (segment between the posterior 1/3 and posterior 1/5) (ISTH) and the splenium (most posterior 1/5). Finally, the splenium was segmented into three equal portions based on its maximal straight length (SPL1–3).

All ROIs were examined for registration errors, which were found in 23 of the 395 participants. Registration errors typically reflected an overestimation of the superior border of the posterior genu and anterior/mid-body regions of the CC. For these 23 cases, each anatomically misaligned ROI was manually edited by two independent raters (CA and JL) who attained excellent agreement: mean Dice similarity coefficient = 0.98 (Dice 1945).

The image processing began by applying the fMRI Software Library (FSL) linear and nonlinear co-registration tools, FLIRT (with 6 degrees of freedom) and FNIRT (Jenkinson et al. 2012) to co-register the T_1-weighted image to the first echo of the GRASE dataset and the MNI-152 template brain, respectively. The inverse of the warp-field transformation from the above step was applied to each CC region (in MNI-152 space). These subject-space ROIs were then applied to each of the 32 echoes of the GRASE sequence using FSLMATHS tool. The T_1-weighted images were segmented to generate tissue-probability maps of white matter, gray matter, and cerebrospinal fluid using the FSL segmentation tool (Zhang et al. 2001), which assigns each voxel, a probability of belonging to one of the three tissue types. The obtained white-matter probability maps were then co-registered to the same space as the GRASE images. To ensure that each CC region consisted primarily of white matter, the white matter probability maps were thresholded and binarized to generate a mask reflecting probability values of 95% or greater, which was then multiplied by each CC region for each subject. The ROI masks in subject space were co-registered to the GRASE images.

To estimate the multiple T_2 components in each pixel within each ROI, a regularized nonnegative least squares (rNNLS) algorithm (Whittall et al. 2002) was applied as detailed in our previous publication (Arshad et al. 2017). Generalized cross validation was used to find the optimal regularization parameter (Golub et al. 1979). The extended phase graph algorithm was included as part of the rNNLS fitting procedure to control for nonideal refocusing flip angles (Henning 1988; Prasloski et al. 2012). Distributions of the T_2 relaxation components were generated using 200 logarithmically spaced T_2 values ranging between 10 and 2000 ms. MWF was defined as the total amplitude of T_2 components between 10 and 40 ms relative to the total amplitude of all T_2 components (expressed as a percent). $geomT_{2IEW}$ was defined as the geometric mean of the T_2 component distribution

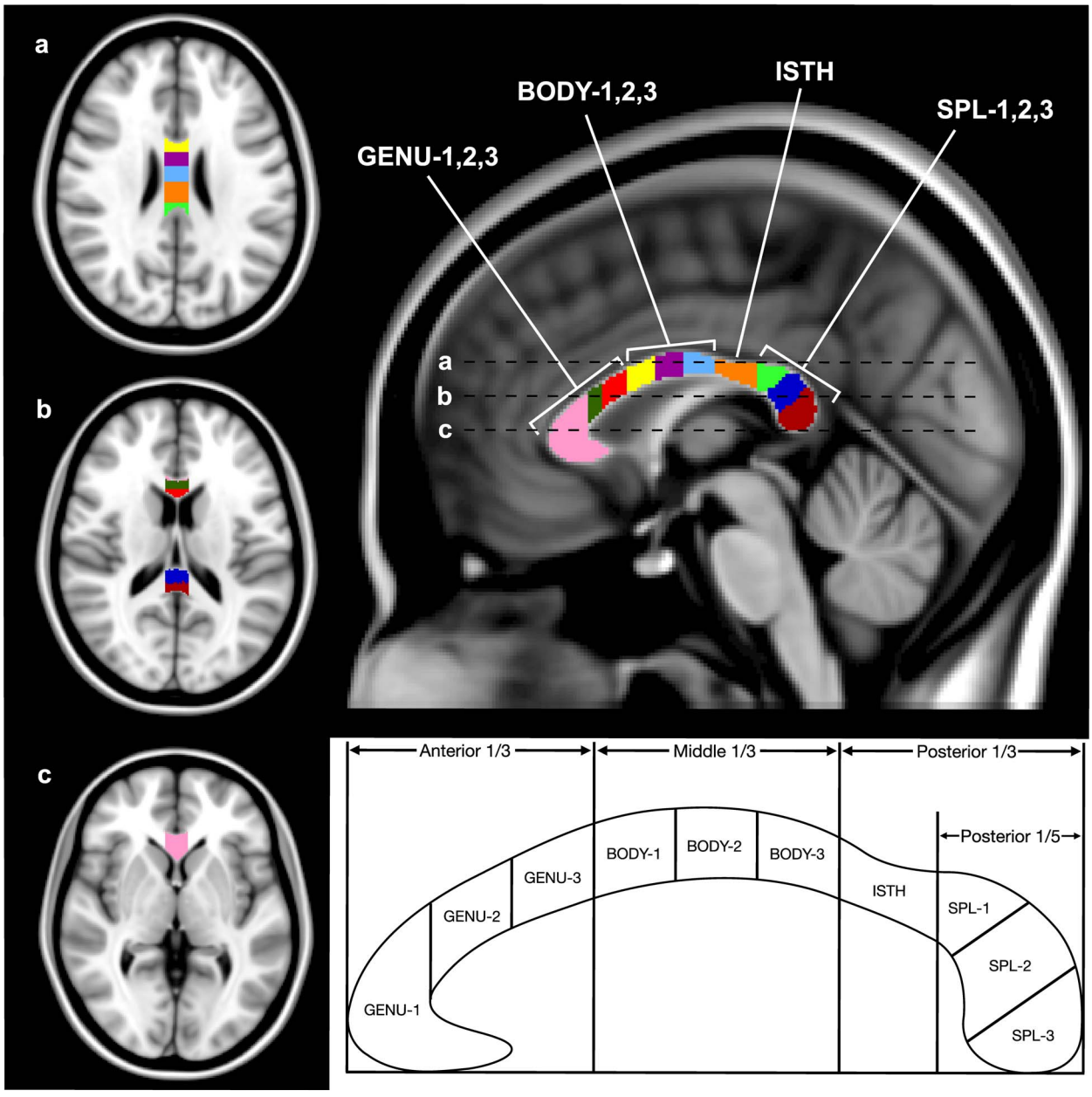

Figure 1. Axial and midsagittal views of the CC, with 10 ROIs shown in MNI-152 standard space. The regions, from right to left: GENU-1 (pink), GENU-2 (dark green), GENU-3 (red), BODY-1 (yellow), BODY-2 (purple), BODY-3 (light blue), ISTH (orange), SPL-1 (light green), SPL-2 (dark blue), and SPL-3 (dark red). The three lines (a, b, and c) on the midsagittal view represent the location of the three axial slices displayed on the left. Schematic showing the division of the CC into 10 ROIs is shown below. The anterior and middle thirds of the CC were divided into three equal portions representing the three segments of the genu and body, respectively. The space between the beginning of the posterior 1/3 and the posterior 1/5 was designated as the isthmus, and the anterior 1/5 was divided into three equal segments (based on straight length) for the three segments of the splenium.

between T_2 values of 40–200 ms (typically between 50 and 80 ms) [see Fig. 1 in Arshad et al. (2016)]. In each ROI, the MWF and geomT_{2IEW} values reflect the average of all pixels with a white matter probability value of 95% or greater.

Statistical Analyses

To assess regional, age, and sex differences in MWF and geomT_{2IEW} we used the general linear model (GLM) framework in two separate models. In each model, MWF or geomT_{2IEW} was the dependent variable with ROI being a within subject, 10-level factor, and sex—a between-subject categorical factor. Age, centered at the sample mean, and squared mean-centered age were continuous independent variables. Interactions between the continuous variables and sex were tested to ensure homogeneity of regression, and, if found nonsignificant ($P > 0.10$), dropped from the model. The Huynh-Feldt correction was applied to offset the violation of sphericity assumption. If the interactions age^2 × ROI or age × ROI were significant, GLM analyses were followed up by piecewise regressions of

Table 1 Summary of GLM analyses of age differences in MWF and geomT$_{2IEW}$ across CC regions

		Age				Age^2			
Dependent variable	Region	Overall adjusted R^2	*b*	ß	*P*	Overall adjusted R^2	*b*	ß	*P*
MWF	GENU-1	0.21	0.068	0.45	<**0.001**	0.34	−0.0040	−0.65	<**0.001***
	GENU-2	0.11	0.037	0.34	<**0.001**	0.24	−0.0028	−0.63	<**0.001***
	GENU-3	0.15	0.043	0.39	<**0.001**	0.26	−0.0027	−0.61	<**0.001***
	BODY-1	0.23	0.055	0.48	<**0.001**	0.31	−0.0025	−0.53	<**0.001***
	BODY-2	0.24	0.064	0.50	<**0.001**	0.34	−0.0030	−0.56	<**0.001***
	BODY-3	0.25	0.066	0.50	<**0.001**	0.38	−0.0036	−0.66	<**0.001***
	ISTH	0.35	0.084	0.60	<**0.001**	0.42	−0.0026	−0.45	<**0.001***
	SPL-1	0.44	0.11	0.66	<**0.001**	0.49	−0.0028	−0.41	<**0.001***
	SPL-2	0.48	0.14	0.69	<**0.001**	0.54	−0.0037	−0.45	<**0.001***
	SPL-3	0.35	0.12	0.59	<**0.001**	0.39	−0.0032	−0.38	<**0.001***
geomT$_{2IEW}$	GENU-1	0.49	0.078	0.70	<**0.001***	0.49	0.000059	0.11	0.08
	GENU-2	0.15	0.043	0.40	<**0.001***	0.16	0.00059	0.13	0.11
	GENU-3	0.12	0.036	0.34	<**0.001***	0.13	0.00089	0.21	0.01
	BODY-1	0.09	0.031	0.31	<**0.001***	0.10	0.00063	0.15	0.08
	BODY-2	0.05	0.025	0.23	<**0.001***	0.06	−0.00056	−0.12	0.16
	BODY-3	0.01	0.0095	0.09	0.07	0.03	−0.0011	−0.27	**0.003***
	ISTH	0	0.00028	0.0026	0.96	0	0.00054	0.13	0.17
	SPL-1	0.09	0.031	0.30	<**0.001***	0.08	0.000012	0.06	0.75
	SPL-2	0.27	0.067	0.52	<0.001	0.29	−0.0016	−0.30	<**0.001***
	SPL-3	0.12	0.050	0.35	<0.001	0.15	−0.0019	−0.33	<**0.001***

Note: *ROI's with a significant age effect after correcting for multiple comparisons.

the dependent variable on age, to establish the contribution of linear and quadratic trends in each ROI individually. With 10 possible regressions in the post hoc analysis, the nominal α level of 0.05 was adjusted to $\alpha' = 0.005$ using the Bonferroni correction.

Although this sample spanned an age range of 7–85 years (M = 30.8, SD = 21.9), the two age extremes were over-represented, with relatively few participants between 30 and 50 years (N = 20, 5% of the sample). Therefore, for follow-up analyses of significant quadratic age-affects the sample was split into two bins based on the age, at which the quadratic line of fit peaked for each ROI. Separate linear regression models were fit to the data on the subjects with values falling on either side of the peak, for each ROI.

To minimize rounding errors and scaling artifacts, the MWF values were multiplied by 100 and expressed as percentages, whereas the geomT$_{2IEW}$ values that were expressed in milliseconds were multiplied by 1000. All statistical analyses were conducted using R (version 3.5.2), SAS JMP (version 14), and SYSTAT (version 13) packages.

Results

Regional and Age Differences in MWF

GLM analyses revealed a significant main effect of ROI [$F(9,3528) = 261.87$, $P < 0.001$], age [$F(1,391) = 319.54$, $P < 0.001$ and age^2 [$F(1,391) = 91.18$, $P < 0.001$], but not sex [$F(1,391) = 0.099$, $P = 0.75$]. Age effects were conditioned, however, on significant interactions with ROI: Age × ROI [$F(9,3528) = 30.42$, $P < 0.001$] and Age^2 × ROI [$F(9,3528) = 3.21$, $P < 0.001$]. Significant linear and quadratic relationships between MWF and age were observed in all 10 ROIs (Table 1; Fig. 2); however, the improved R^2 values in the quadratic MWF fits reflect an improvement upon the linear fits for each ROI (Table 1).

Myelin content (MWF) differed across the regions. It increased from the anterior to posterior end of the CC, with the lowest in the anterior, middle, and posterior genu (GENU-1: M = 9.86, SD = 3.31; GENU-2: M = 8.32, SD = 2.42; GENU-3: M = 8.20, SD = 2.41) and anterior body (BODY-1: M = 8.36, SD = 2.52), and the highest in the three segments of the splenium (SPL-1: M = 11.3, SD = 3.7; SPL-2: M = 12.7, SD = 4.4; SPL-3: M = 16.8, SD = 4.6). This general trend of MWF increasing along the anterior–posterior extent of the CC was observed across the entire age range.

The age at which MWF peaked was calculated as the x-coordinate corresponding to the vertex of the quadratic line of fit and is as follows for each ROI: GENU-1 = 49.4, GENU-2 = 47.5, GENU-3 = 48.9, BODY-1 = 52.1, BODY-2 = 51.9, BODY-3 = 50.3, ISTH = 57.2, SPL-1 = 60.3, SPL-2 = 59.6, SPL-3 = 59.9 years (Table 2). The age at peak MWF was used as the dividing value to form the two bins for each ROI. Thus, each ROI had its own age bins, depending on the peak value observed in that region, which ranged between 47.5 and 60.3 years for MWF. Follow-up analyses on the pre- and postpeak age bins revealed that the observed full-sample quadratic association of MWF with age was driven entirely by a robust linear relationship between MWF and age in the younger (prepeak), with nonsignificant linear trends after adjusting for multiple comparisons for each ROI among the older (postpeak) participants (Table 2). The Brown-Forsythe test revealed no differences in the variance across the bins for each ROI.

Regional and Age Differences in geomt$_{2iew}$

The geomT$_{2IEW}$ showed a significant main effect of ROI [$F(9,3528) = 410.33$, $P < 0.001$] and age [$F(1,391) = 31.86$, $P < 0.001$], but neither age^2 [$F(1,391) = 0.42$, $P = 0.5$] nor sex [$F(1,391) = 0.13$, $P = 0.7$]. The significant interaction terms age × ROI [$F(9,3528)$

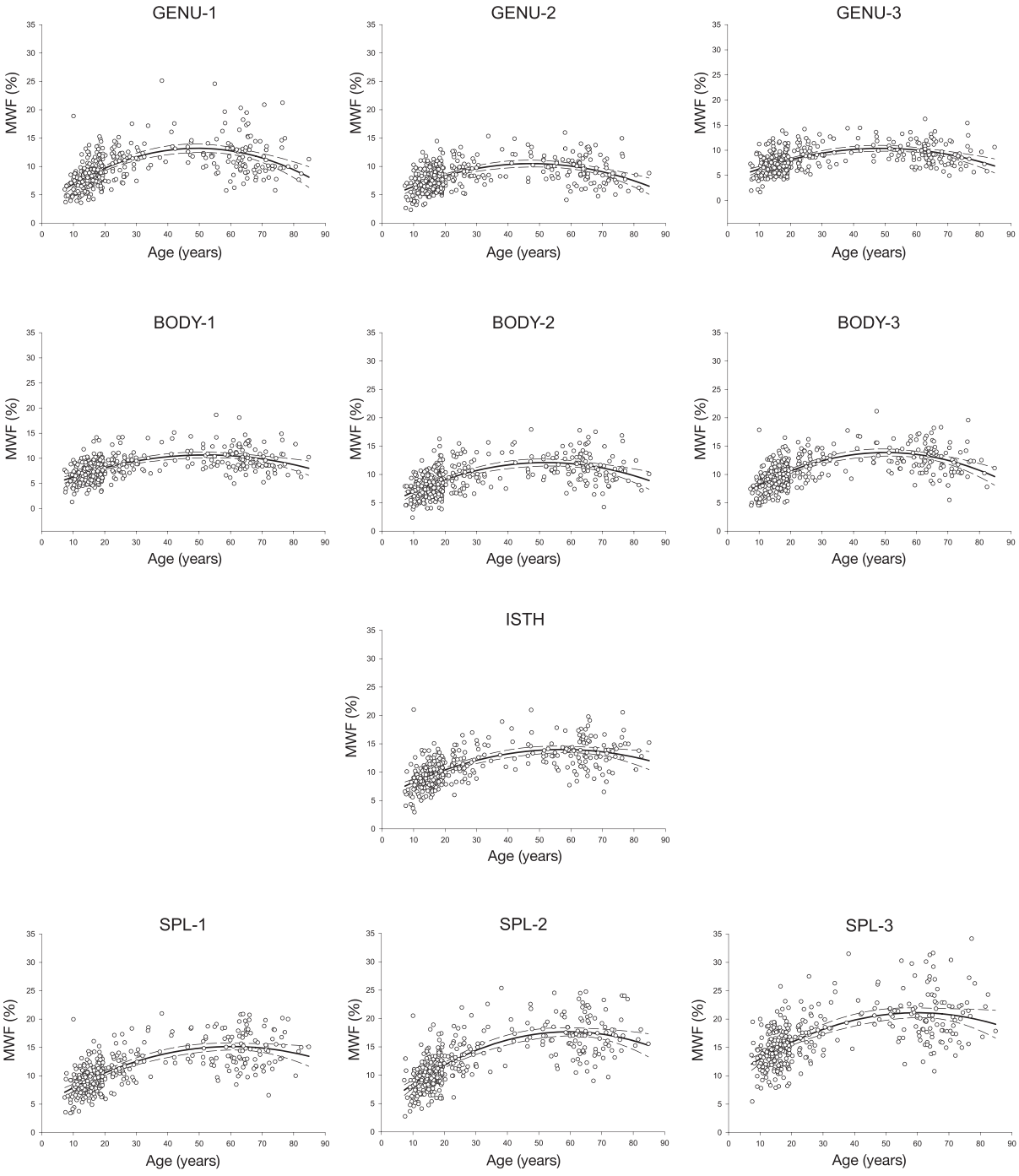

Figure 2. MWF (%) averaged within each ROI, from anterior to posterior (left to right) for the full sample plus the two age groups defined by the age at the peak value. The error bars represent ±99% confidence intervals (CIs).

$= 30.59$, $P < 0.001$] and age^2 × ROI, [$F(9,3528) = 16.97$, $P < 0.001$] indicated, however, regional differences in the pattern of geomT$_{2IEW}$ associations with age.

Among the regional geomT$_{2IEW}$ values (Fig. 5), the lowest was in the anterior genu (GENU-1: M = 60.4, SD = 2.4), with an increase along the anterior-poster axis, peaking at the posterior body (BODY-3: M = 70.2, SD = 2.3), declining until the middle splenium (SPL-2: M = 64.4, SD = 2.8), followed by a small uptick in the most posterior region of the splenium (SPL-3: M = 65.9, SD = 3.2).

Follow-up regressions on age for each ROI showed significant associations between age and geomT$_{2IEW}$ in all regions except the posterior body [BODY-3: $F(1,392) = 3.26$, $P = 0.07$] and the isthmus [ISTH: $F(1,392) = 0.003$, $P = 0.96$] (Table 1, Fig. 4). Significant quadratic relationships between geomT$_{2IEW}$ values and age were observed in the BODY-3, SPL-2, and SPL-3 ROIs as noted in Table 1 (Fig. 4). Applying a similar binning approach as the MWF quadratic fits, the ages at which the geomT$_{2IEW}$ peaked for the BODY-3, SPL-2, and SPL-3 were 45.1, 62.6, and 53.7 years,

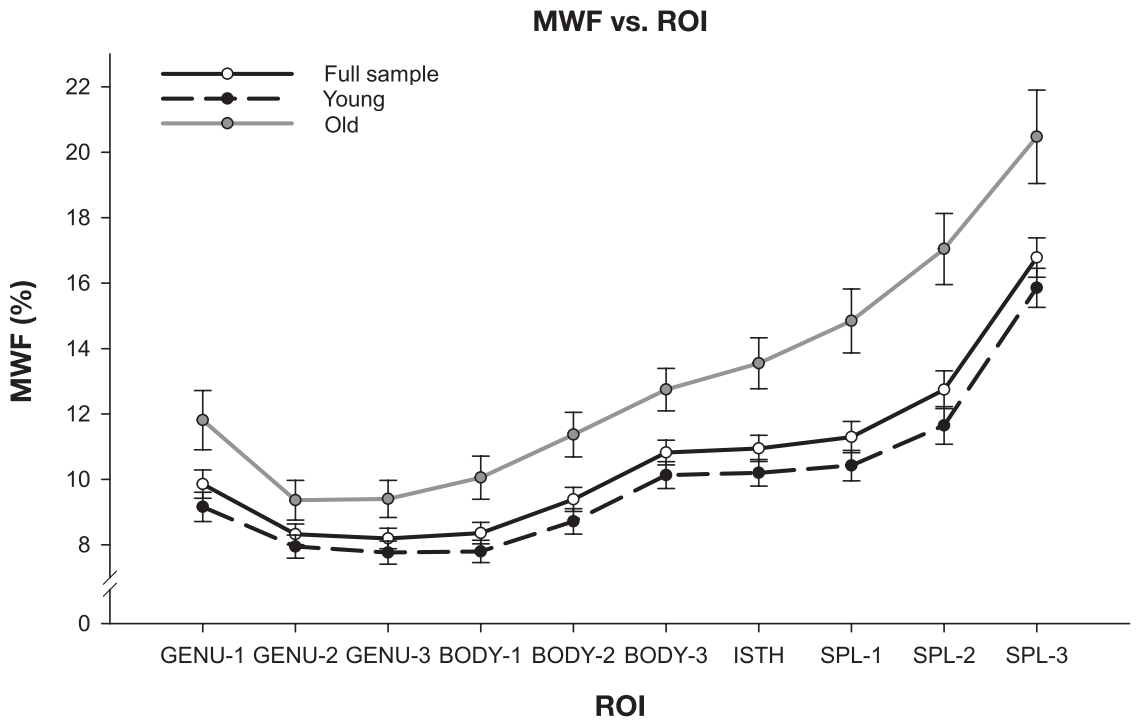

Figure 3. MWF (%) plotted against age for each ROI. MWF data were best fit by a quadratic function across the lifespan and the ±99% CIs are marked by the dashed lines.

respectively (Table 2). Follow-up analyses on the pre- and post-peak age bins for these three ROI's revealed that the quadratic relationship between age and geomT_{2IEW} was driven by a significant positive linear relationship in the young, with only nonsignificant linear effects of age in the old (Table 2). These trends were similar to those observed for MWF. The Brown-Forsythe test revealed no differences in the variance across the age bins for the BODY-3 and SPL-2; whereas significantly inhomogeneity of variances across the age bins were noted for the SPL-3 [$F(1,392) = 7.29$, $P = 0.007$].

Discussion

Regional Differences in Callosal Microstructure

We observed substantial regional differences in white matter properties of the human CC with the lowest myelin content in the genu followed by intermediate values in the body/isthmus and the highest values in the splenium. The discrepancy in MWF between the genu and splenium amounted to ~30%, as illustrated in Figures 2 and 6. A similar pattern of myelin content differences across the CC of healthy adults has been reported using ME-T_2 combined with multi-T_2 component fitting (Friedrich et al. 2020). In contrast, Björnholm et al. (2017) reported the highest MWF values in the genu and the lowest in the body. The inconsistency may stem from the use of the mcDESPOT, an approach that has been criticized for confounding magnetization transfer effects (Zhang et al. 2015) and the influence of water exchange between the different compartments (Lankford and Does 2013; Does 2018; West et al. 2019). In addition, as expected, conventional DTI-derived indicators also evinced different patterns across the CC in healthy individuals (Hasan et al. 2005; Hofer and Frahm 2006; Rittner et al. 2014). The inconsistency between MWF and DTI findings is supported by the literature (Billiet et al. 2015; Arshad et al. 2016; Faizy et al. 2020) and is unsurprising considering that anisotropic water diffusion is influenced by multiple factors including axon caliber, axon density, myelination, fiber orientation, presence of crossing fibers, and permeability of cell membranes. (Jones and Cercignani 2010; Jones et al. 2013). Interestingly, histological studies on macaques and human postmortem material (Aboitiz et al. 1992) have reported increasing mean axon diameter from the genu to the splenium—a pattern observed here for MWF. Therefore, MWF, in addition to measuring myelin content (Webb et al. 2003; Laule et al. 2006; Laule et al. 2008; McCreary et al. 2009), may also indirectly reflect differences in the average diameter of all axons within the region of interest, which is a novel observation. This may stem from the association between axon diameter and the thickness of the myelin sheaths: as the axon caliber increases, so does the thickness of the lamina. Clarification of the dual role of MWF as a marker of myelin content, for which it has been validated, and an index of average axon diameter warrants a histological study.

In contrast to MWF, the regional profile of geomT_{2IEW} demonstrated the highest values in the posterior body (BODY-3) followed by the isthmus (Fig. 5). The lowest geomT_{2IEW} values were in the genu and the middle portion of the splenium (SPL-2). The discrepancy in patterns of regional differences between MWF and geomT_{2IEW} across regions suggests distinct attributes in the characterization of the white matter microstructure. This is not surprising because the callosal white matter is highly heterogeneous with respect to axon density, diameter (or thickness), and interaxon distance (LaMantia and Rakic 1990a; Aboitiz et al. 1992). Specifically, small axons (under 1 µm in diameter) account for approximately 80% of total fibers, with the highest density in the genu and the middle portion of the splenium (SPL-2) and

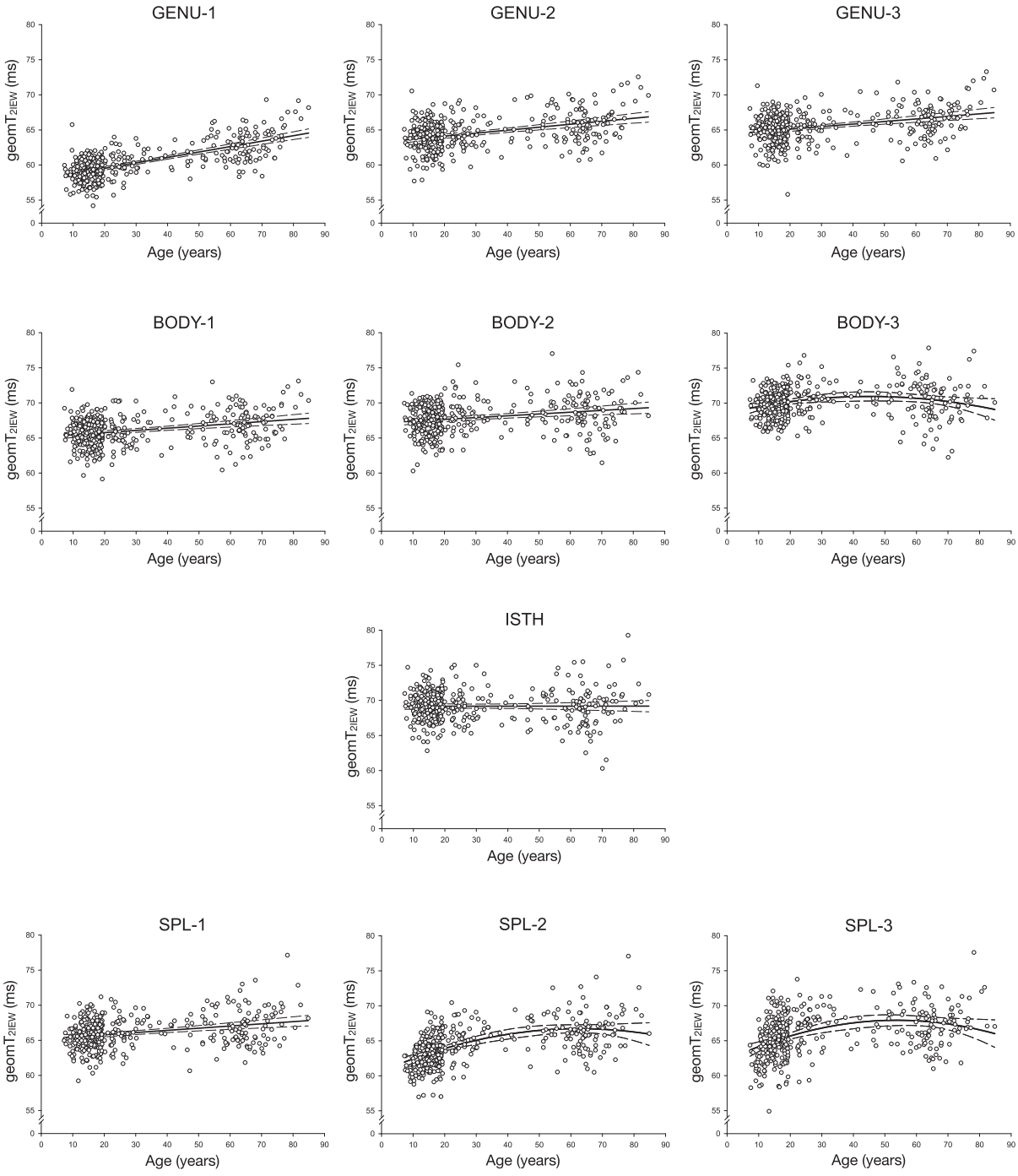

Figure 4. geomT$_{2IEW}$ (ms) plotted against age for each CC ROI. The pattern of geomT$_{2IEW}$ across the lifespan was best described by a linear function in most ROIs, except the posterior body (BODY-3) and the isthmus (ISTH), which did not exhibit a significant linear relationship between geomT$_{2IEW}$ and age. The ±99% CIs are represented by the dashed lines.

the lowest in the posterior body (BODY-3). The distribution is mirrored for the largest (>5 µm in diameter) axons, which show the highest density in the BODY-3 and are absent in the GENU-1. Thus, the geomT$_{2IEW}$ is remarkably consistent in predicting the contribution of large-diameter axons in the regions, that also show greater interaxon distances (Fig. 5).

As the contribution of larger axons (>5 µm) increases, overall axon density decreases. This amounts to a 25% drop in axon density between the GENU-1 and BODY-3 (Aboitiz et al. 1992), and coincides with an increase in the interaxon distance thus leading to expansion of the extra- and intracellular space. This spatial expansion is consistent with higher geomT$_{2IEW}$ values that reflect increased water mobility (Carr and Purcell 1954; Meiboom and Gill 1958; MacKay et al. 1994; Whittall et al. 1997; Does 2018). The decrease in density in regions with a greater share of larger axons may also explain the dissociation between

Table 2 Descriptive statistics for the two age bins and age differences in MWF and geomT$_{2IEW}$ within peak-related age bins (prior and after peak)

Dependent variable	Region	Peak age (years)	Before peak					After peak				
			N (% females)	Overall adjusted R^2	*b*	*ß*	*P*	N (% females)	Overall adjusted R^2	*b*	*ß*	*P*
MWF	GENU-1	49.4	291 (59)	0.35	0.22	0.59	**<0.001**	104 (62)	0.02	−0.07	−0.14	0.15
	GENU-2	47.5	290 (59)	0.23	0.15	0.48	**<0.001**	105 (62)	0.04	−0.07	−0.23	0.02
	GENU-3	48.9	291 (59)	0.25	0.15	0.50	**<0.001**	104 (62)	0.02	−0.06	−0.20	0.04
	BODY-1	52.1	297 (59)	0.24	0.12	0.49	**<0.001**	98 (61)	0.01	−0.06	−0.18	0.08
	BODY-2	51.9	295 (59)	0.25	0.15	0.51	**<0.001**	100 (61)	0.02	−0.07	−0.19	0.06
	BODY-3	50.3	291 (59)	0.34	0.20	0.59	**<0.001**	104 (62)	0.01	−0.06	−0.18	0.07
	ISTH	57.2	307 (59)	0.31	0.14	0.56	**<0.001**	88 (61)	0	0.02	0.04	0.73
	SPL-1	60.2	317 (59)	0.39	0.16	0.62	**<0.001**	78 (63)	0	0.02	0.03	0.79
	SPL-2	59.6	315 (59)	0.46	0.22	0.68	**<0.001**	80 (61)	0.01	0.05	0.07	0.51
	SPL-3	59.9	316 (59)	0.36	0.20	0.60	**<0.001**	79 (62)	0	0.08	0.09	0.42
geomT$_{2IEW}$	BODY-3	45.1	284 (58)	0.30	0.0022	0.56	**<0.001**	111 (62)	0.04	−0.00073	−0.24	0.01
	SPL-2	62.6	327 (59)	0.43	0.0018	0.66	**<0.001**	68 (62)	0.01	−0.00011	−0.16	0.90
	SPL-3	53.74	298 (59)	0.32	0.0024	0.57	**<0.001**	97 (61)	0	0.00020	0.028	0.78

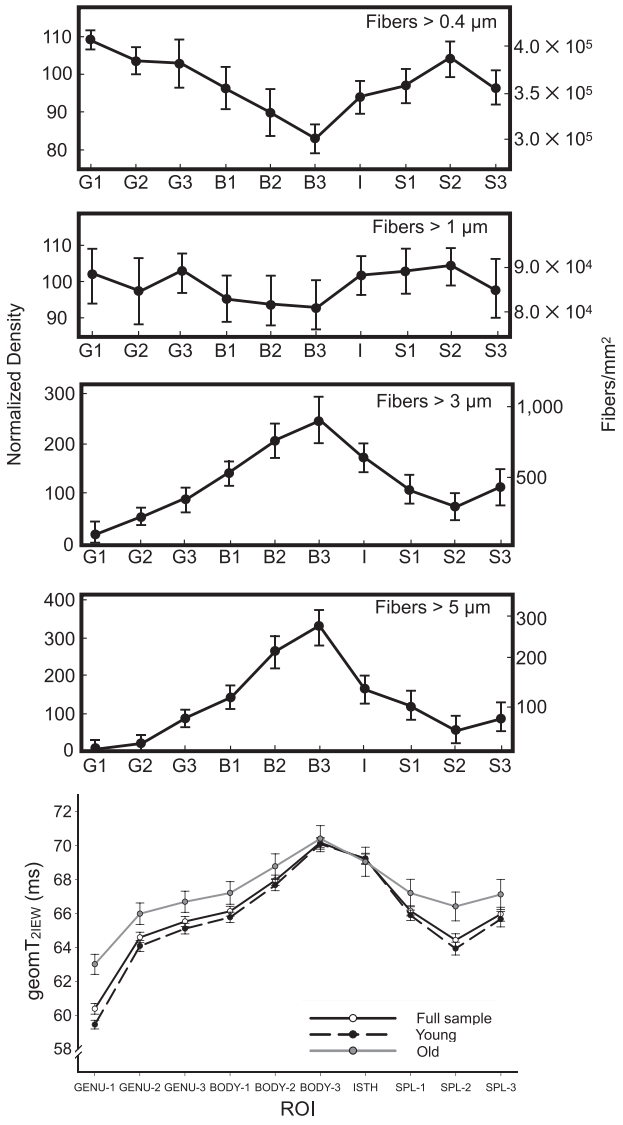

Figure 5. The first four plots are adapted from Aboitiz et al. (1992). The distribution of large diameter fibers (>3 µm and > 5 µm) closely resembles the pattern of geomT$_{2IEW}$ across all ROIs (bottom) for the full sample plus the two peak-dependent age groups. Error bars in Aboitiz's graphs represent ±1 SD and the error bars in the geomT$_{2IEW}$ plot represent ±99% CIs.

MWF and geomT$_{2IEW}$. That is, larger axons tend to have thicker myelin lamina, and therefore greater myelin content. However, it appears that increases in interaxon distance disengages the association between large axons and high MWF values. For example, MWF is higher in the splenium than in the body. Collectively, the surveyed evidence bolsters the validity of ME-T$_2$ imaging combined with multi-T$_2$ component fitting as a tool for evaluating the white matter microstructure in vivo, including independent assessment of myelin content (average axon diameter driven by small-caliber axons) and contribution of large fibers (or packing density).

The profile of regional differences in geomT$_{2IEW}$ observed in our study also diverges from the one reported by Björnholm et al. (2017), where MWF, and to a lesser extent R$_2$ values (inverse of geomT$_{2IEW}$), closely corresponded to the histological regional distribution of small-caliber densely packed axons (>0.4 µm)

(Aboitiz et al. 1992). As noted above, the reason for this discrepancy is unclear aside from somewhat different acquisition and modeling methods applied in that study (Does 2018), as well as limiting the lateral extent of the CC to a single mid-sagittal slice. Interestingly, a recent study using multishell diffusion-weighted imaging, which has the ability to separate relatively fast and slow water diffusion compartments, has reported a profile of regional differences that is similar to the one observed here (Genc et al. 2018). In that study, the apparent fiber density (AFD) metric matched our $geomT_{2IEW}$ profile and the distribution of larger axons (>5 μm) reported in histological investigation (Aboitiz et al. 1992). This agreement bolsters the likelihood of $geomT_{2IEW}$ reflecting the contribution (or packing density) of large-diameter fibers in white matter as we propose.

With respect to the regional differences in CC microstructure, we can summarize that segments projecting from association cortices displayed lower MWF and $geomT_{2IEW}$ values, as would be predicted from the preponderance of densely packed, small-diameter fibers and hence, lower myelin content and reduced water mobility in the restricted intra- and extracellular space. On the other hand, CC regions containing the axons connecting primary sensory and motor cortices showed higher $geomT_{2IEW}$ values. This is consistent with increased water mobility in an expanded intra- and extracellular space, and presence of large-diameter axons with greater interaxon distances. Thus, in addition to its high reliability (Anand et al. 2019), $geomT_{2IEW}$ emerges as a sensitive index of white matter microstructure suitable for the future in vivo examination of its correlates. In addition, the trend of increasing average axon diameter from the genu to the splenium (LaMantia and Rakic 1990a; Aboitiz et al. 1992), mirroring the relative trend observed in the MWF, supports the proposition that MWF reflects myelin content driven potentially by the average diameter of fibers in white matter tissue.

Histological studies support the plausibility of a strong structure–function correspondence that supports specialization of the callosal regions (Pandya et al. 1971; Barbas and Pandya 1984; Cipollon and Pandya 1985; de Lacoste et al. 1985; Alexander and Warren 1988; LaMantia and Rakic 1990b). Nonetheless, only a direct investigation of the associations between behavioral indicators and regional CC structure can test these hypotheses. The indicators employed in this study may be particularly well suited for such studies.

Lifespan Age Differences in Callosal Microstructure

Myelin content estimated by MWF varied substantially across the wide age range sampled in this study. The age at which MWF reached the highest values also varied across regions (47–60 years), with more anterior regions peaking earlier than posterior ones. Although in the full sample, age-differences were best described by a quadratic function, follow-up analyses revealed that this nonlinearity primarily reflected a steep linear increase in myelin content from childhood to middle age followed by a plateau in the elderly. The magnitude of the MWF difference between the very young and those around the age at which MWF peaked was somewhat similar across the regions (Fig. 6) with no stark contrast between regions related to primary sensory and association cortices (e.g., genu and splenium) as reported by Aboitiz et al. (1996). In the older participants, none of 10 CC regions exhibited significant associations between age and MWF. This contrast between the younger and older individuals is consistent with rapid myelination of the CC early in the lifespan that continues, to some extent, into adulthood with little to no evidence for decline in older age. Processes involved in the maturation of white matter include increased axonal caliber leading to a thicker myelin lamina (Friede and Samorajski 1970; Lee and Cleveland 1994; Sanchez et al. 1996). Therefore, the age-related increase in MWF may be driven by the expected age-related increase in axon diameter and hence, thicker myelin lamina, as also reported by Aboitiz et al. (1996).

The timing of the transition between continued maturation and the onset of aging is controversial. In the absence of longitudinal studies, postmortem investigations (Lintl and Braak 1983; Tang et al. 1997; Peters 2002; Peters and Sethares 2002; Marner et al. 2003) and in vivo findings (Billiet et al. 2015; Arshad et al. 2016; Faizy et al. 2020) do not show clear consistency. The age at this inflection point between rapid MWF growth and stabilization (or weak decline) is also region-dependent, with the genu peaking the earliest (47–49 years) and the splenium the latest (60 years). Of note, in a sample of healthy adults, Faizy et al. (2020) reported a negative relationship between MWF and age in the genu and splenium, whereas no associations between MWF and age were detected in the genu or splenium by Billiet et al. (2015). In addition, whereas quadratic age relationships with DTI indices have been reported in some studies of healthy adolescents/adults, the peak values correspond to much earlier ages, ranging between 20 and 39 years (Hasan et al. 2009; Westlye et al. 2010; Bartzokis et al. 2012; Lebel et al. 2012; Billiet et al. 2015; Kochunov et al. 2016). Others have not found quadratic relationships between DTI indices and age at all (Salat, et al. 2005b; Faizy et al. 2020). Our findings, however, support the postmortem evidence suggesting that myelination continues well into adulthood, albeit not at the magnitude observed in children (Kaes 1907; Yakovlev and Lecours 1967; Miller et al. 2012). The conflicting results between age effects in MWF and DTI indices suggest, as noted above, that processes other than myelination may be driving the earlier inflection point observed in DTI studies. Moreover, because all of the cited studies including the current are cross-sectional and are incapable of capturing the individual differences in change, the true trajectories of myelination and changes in axon diameter/packing density, especially in older adults, remain unknown.

In contrast to MWF, $geomT_{2IEW}$ exhibited a linear increase with age within 7 of the 10 CC ROIs. These linear associations indicate increased water mobility in the intra- and extracellular space in the older brains. The microstructural mechanisms responsible for these age differences may vary across the lifespan. In the younger group, the age-related rise in $geomT_{2IEW}$ values is consistent with increased axonal caliber concomitant with increased interaxon distance (or decreased packing density) during the white matter maturational process (Friede and Samorajski 1970; Lee and Cleveland 1994; Sanchez et al. 1996). This is also in accord with the observed period of rapid increase in MWF with age that also reflects maturation as discussed above. Conversely, a continuing increase in $geomT_{2IEW}$ concomitant with little, if any, differences in MWF or weak trends of MWF decline in the older group (Fig. 6) is in line with evidence of axonal degeneration and loss described in the postmortem literature (Lintl and Braak 1983; Meier-Ruge et al. 1992; Tang et al. 1997; Peters 2002; Peters and Sethares 2002; Marner et al. 2003; Hou and Pakkenberg 2012). In the older group, the degeneration of axons disrupts the myelin sheaths. The resulting increase in cytoplasmic inclusions may lead to relatively higher $geomT_{2IEW}$ values stemming from the heightened mobility of water in the cytoplasm between sheaths and decreased fiber density, as observed.

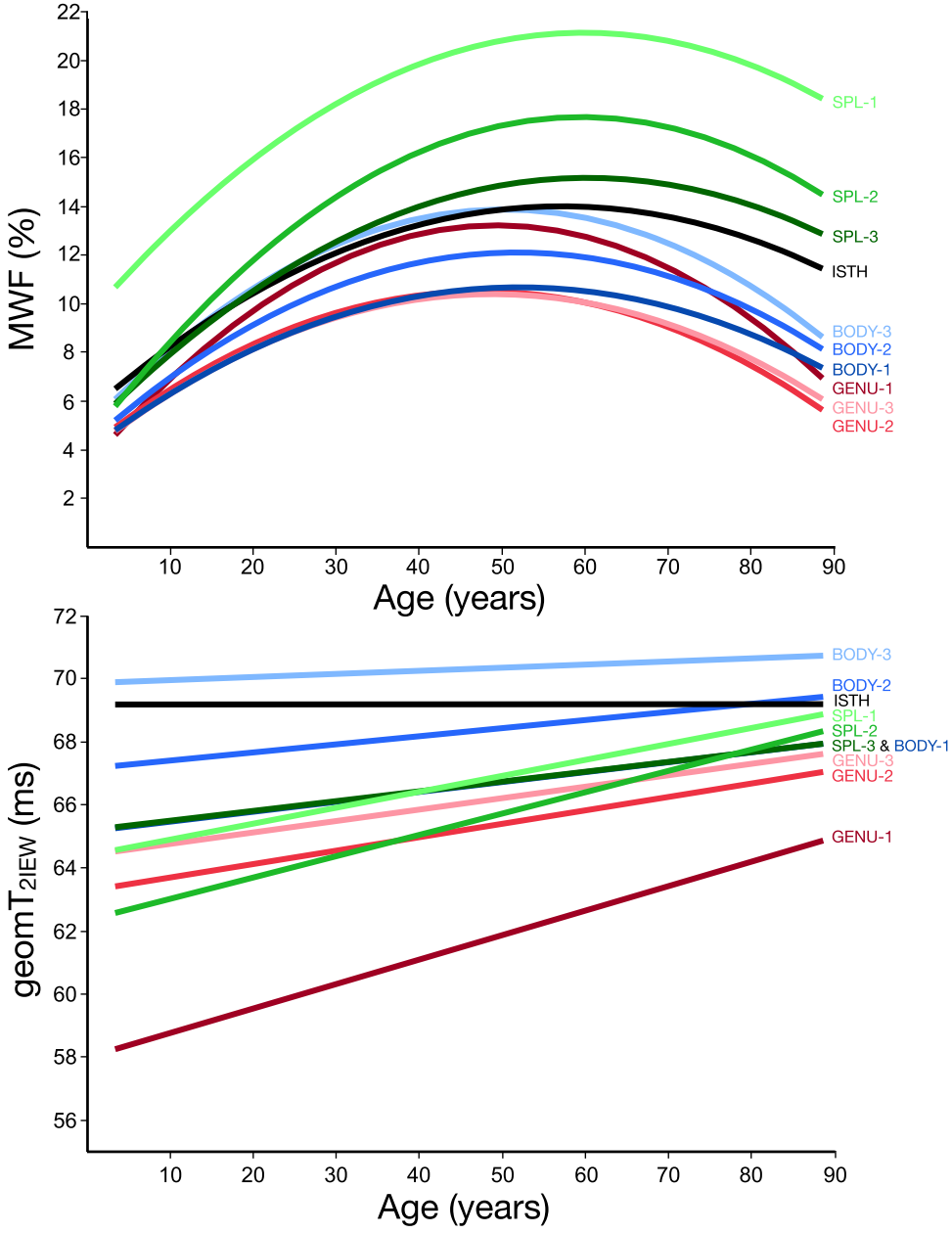

Figure 6. MWF (%) (top) and geomT$_{2IEW}$ (ms) (bottom) best fit curves for each CC ROI plotted against age.

The most pronounced age differences in geomT$_{2IEW}$ (and to a lesser degree in MWF) were found in the genu of the CC. This observation is in line with histological (Aboitiz et al. 1996; Hou and Pakkenberg 2012) and in vivo studies of the white matter microstructure (Fan et al. 2019) as well as the earlier volumetric (Raz et al. 1997; Raz et al. 2005) and DTI (Head et al. 2004) reports that suggest an anterior-to-posterior gradient of white matter aging. The selective susceptibility of the genu—a CC region, whose fibers connect right and left prefrontal areas—to aging conforms to the view of these regions being at the cusp of age-related cognitive decline (West 1996; Raz 2000).

Interestingly, in the BODY-2, SPL-2, and SPL-3 geomT$_{2IEW}$ data were best fit with a quadratic function. The trajectory in these regions was similar to that of MWF, with increasing geomT$_{2IEW}$ until the middle age range at which point it appears to level off. The posterior body is thought to contain axons extending from the primary auditory cortices (de Lacoste et al. 1985), whereas the two posterior segments of the splenium carry axons adjoining the visual cortices of either hemisphere (Aboitiz et al. 1992). It is possible, therefore, that these primary sensory cortices and their efferent axons are not as vulnerable to the deleterious effects of aging as are the association regions of the frontal cortex whose axons extend through the genu. The relationship between geomT$_{2IEW}$ and age leveling off in the SPL-2 and SPL-3 may reflect the anterior to posterior gradient of aging postulated by others.

The discrepancy between the current results and the post-mortem evidence of age-related myelin loss could be explained

by a sustained formation of myelin in the healthy elderly that keeps pace with the rate of myelin degradation, and axonal loss, despite accumulating structural deficits in the myelin sheath (Peters 2002). With these two processes being in a dynamic equilibrium, no substantial net myelin decrease would be observed, as is suggested by the observations of the current study. Only pathological aging would be expected to exhibit violation of that equilibrium and substantial myelin depletion (Bartzokis 2004).

The findings reported here should be interpreted in the context of design and sampling limitations. First, cross-sectional studies cannot estimate true change and individual differences therein and cannot act as a substitute for longitudinal studies of life-span development (Raz and Lindenberger 2011). Second, although $geomT_{2IEW}$ is associated with histologically derived regional fiber distributions, it may still be too coarse an indicator of the multifarious alterations in the axon caliber and structure and the mixture of myelinated and unmyelinated axons in a given region. Third, a relative scarcity of middle-aged participants makes conclusions about this segment of the lifespan less reliable than those that pertain to the very well represented young and elderly individuals. Further investigations pitting MRI findings against postmortem histology are needed for clarifying the neurobiological nature of that index, and special efforts in recruiting middle-aged participants are warranted for improving our understanding of the age differences in that segment of population.

In summary, MWF and $geomT_{2IEW}$ values demonstrated unique regional differences across the human CC that closely corresponded with histological profiles reported in the literature. This contributes to the validation of the ME-T_2 approach and suggests that these two indicators characterize distinct attributes of the white matter microstructure including mean axonal diameter and density of large-caliber axons. The quadratic association between MWF and age is driven almost exclusively by the increase in myelin content of the dominating small-diameter axons during development and early adulthood, and for some regions, into the middle age. The linear association between $geomT_{2IEW}$ and age was strongest in the genu, where the fibers connect the homologous prefrontal region. In addition, the increased $geomT_{2IEW}$ concomitant with moderate MWF decline, which was most pronounced in the genu, provides evidence of axonal degeneration and loss in the older adults.

Notes

We thank Cheryl Dahle, Dalal Khatib, Philip Easter, and Caroline Zajac-Benitez for technical su pport and assistance in data collection. *Conflict of Interest:* None declared.

Funding

National Institutes of Health (F31-AG058420-01 to C.A., R01-AG011230 to N.R., R21-AG059160 to J.A.S. and N.R., R01MH59299 to D.R.R.); Lycaki-Young Funds from the State of Michigan.

References

Aboitiz F, Rodriguez E, Olivares R, Zaidel E. 1996. Age-related changes in fibre composition of the human corpus callosum: sex differences. *Neuroreport*. 7:1761–1764.

Aboitiz F, Scheibel AB, Fisher RS, Zaidel E. 1992. Fiber composition of the human corpus callosum. *Brain Res*. 598:143–153.

Alexander MP, Warren RL. 1988. Localization of callosal auditory pathways: a CT case study. *Neurology*. 38:802–804.

Anand C, Brandmaier AM, Arshad M, Lynn J, Stanley JA, Raz N. 2019. White-matter microstructural properties of the corpus callosum: test–retest and repositioning effects in two parcellation schemes. *Brain Struct Funct*. 224: 13.

Arshad M, Stanley JA, Raz N. 2016. Adult age differences in subcortical myelin content are consistent with protracted myelination and unrelated to diffusion tensor imaging indices. *Neuroimage*. 143:26–39.

Arshad M, Stanley JA, Raz N. 2017. Test-retest reliability and concurrent validity of in vivo myelin content indices: myelin water fraction and calibrated T1 w/T2 w image ratio. *Hum Brain Mapp*. 38:1780–1790.

Barbas H, Pandya DN. 1984. Topography of commissural fibers of the prefrontal cortex in the rhesus monkey. *Exp Brain Res*. 55:187–191.

Bartzokis G. 2004. Age-related myelin breakdown: a developmental model of cognitive decline and Alzheimer's disease. *Neurobiol Aging*. 25:5–18 author reply 49-62.

Bartzokis G, Lu PH, Heydari P, Couvrette A, Lee GJ, Kalashyan G, Freeman F, Grinstead JW, Villablanca P, Finn JP *et al*. 2012. Multimodal magnetic resonance imaging assessment of white matter aging trajectories over the lifespan of healthy individuals. *Biol Psychiatry*. 72:1026–1034.

Bender AR, Raz N. 2015. Normal-appearing cerebral white matter in healthy adults: mean change over 2 years and individual differences in change. *Neurobiol Aging*. 36:1834–1848.

Bennett IJ, Madden DJ. 2014. Disconnected aging: cerebral white matter integrity and age-related differences in cognition. *Neuroscience*. 276:187–205.

Berbel P, Innocenti GM. 1988. The development of the corpus callosum in cats: a light- and electron-microscopic study. *J Comparat Neurol*. 276:132–156.

Billiet T, Vandenbulcke M, Madler B, Peeters R, Dhollander T, Zhang H, Deprez S, Van den Bergh BR, Sunaert S, Emsell L. 2015. Age-related microstructural differences quantified using myelin water imaging and advanced diffusion MRI. *Neurobiol Aging*. 36:2107–2121.

Bjornholm L, Nikkinen J, Kiviniemi V, Nordstrom T, Niemela S, Drakesmith M, Evans JC, Pike GB, Veijola J, Paus T. 2017. Structural properties of the human corpus callosum: multimodal assessment and sex differences. *NeuroImage*. 152: 108–118.

Borich MR, Mackay AL, Vavasour IM, Rauscher A, Boyd LA. 2013. Evaluation of white matter myelin water fraction in chronic stroke. *Neuroimage Clin*. 2:569–580.

Brodmann K. 1908. Contributions to the histological localisation of the cerebral cortex VI announcement the arrangement of the cortex in humans. *J Psychol Neurol*. 10:229–244.

Carr HY, Purcell EM. 1954. Effects of diffusion on free precession in nuclear magnetic resonance experiments. *Phys Rev*. 94:630–638.

Cipolloni PB, Pandya DN. 1985. Topography and trajectories of commissural fibers of the superior temporal region in the rhesus monkey. *Exp Brain Res*. 57:381–389.

Curnes JT, Burger PC, Djang WT, Boyko OB. 1988. MR imaging of compact white matter pathways. *AJNR Am J Neuroradiol*. 9:1061–1068.

de Lacoste MC, Kirkpatrick JB, Ross ED. 1985. Topography of the human corpus callosum. *J Neuropathol Exp Neurol*. 44: 578–591.

Di Ieva A, Fathalla H, Cusimano MD, Tschabitscher M. 2015. The indusium griseum and the longitudinal striae of the corpus callosum. *Cortex*. 62:34–40.

Dice LR. 1945. Measures of the amount of ecologic association between species. *Ecology*. 26:297–302.

Does MD. 2018. Inferring brain tissue composition and microstructure via MR relaxometry. *NeuroImage*. 182: 136–148.

Dula AN, Gochberg DF, Valentine HL, Valentine WM, Does MD. 2010. Multiexponential T2, magnetization transfer, and quantitative histology in white matter tracts of rat spinal cord. *Magn Reson Med*. 63:902–909.

Faizy TD, Thaler C, Broocks G, Flottmann F, Leischner H, Kniep H, Nawabi J, Schon G, Stellmann JP, Kemmling A *et al*. 2020. The myelin water fraction serves as a marker for age-related myelin alterations in the cerebral white matter - a multiparametric MRI aging study. *Front Neurosci*. 14:136.

Fan Q, Tian Q, Ohringer NA, Nummenmaa A, Witzel T, Tobyne SM, Klawiter EC, Mekkaoui C, Rosen BR, Wald LL *et al*. 2019. Age-related alterations in axonal microstructure in the corpus callosum measured by high-gradient diffusion MRI. *NeuroImage*. 191:325–336.

Flechsig P. 1901. Developmental myelogenetic localization of the cerebral cortex in the human subject. *Lancet*. 158:1027–1030.

Folstein MF, Folstein SE, McHugh PR. 1975. Mini-mental state. A practical method for grading the cognitive state of patients for the clinician. *J Psychiatr Res*. 12:189–198.

Friede RL, Samorajski T. 1970. Axon caliber related to neurofilaments and microtubules in sciatic nerve fibers of rats and mice. *Anat Rec*. 167:379–387.

Friedman AL, Burgess A, Ramaseshan K, Easter P, Khatib D, Chowdury A, Arnold PD, Hanna GL, Rosenberg DR, Diwadkar VA. 2017. Brain network dysfunction in youth with obsessive-compulsive disorder induced by simple uni-manual behavior: the role of the dorsal anterior cingulate cortex. *Psychiatry Res Neuroimaging*. 260:6–15.

Friedrich P, Fraenz C, Schluter C, Ocklenburg S, Madler B, Gunturkun O, Genc E. 2020. The relationship between axon density, myelination, and fractional anisotropy in the human Corpus callosum. *Cereb Cortex*. 30:2042–2056.

Genc S, Malpas CB, Ball G, Silk TJ, Seal ML. 2018. Age, sex, and puberty related development of the corpus callosum: a multi-technique diffusion MRI study. *Brain Struct Funct*. 223:2753–2765.

Golub GH, Heath M, Wahba G. 1979. Generalized cross validation as a method for choosing a good ridge parameter. *Technometrics*. 21:9.

Hasan KM, Gupta RK, Santos RM, Wolinsky JS, Narayana PA. 2005. Diffusion tensor fractional anisotropy of the normal-appearing seven segments of the corpus callosum in healthy adults and relapsing-remitting multiple sclerosis patients. *J Magn Reson Imaging*. 21:735–743.

Hasan KM, Kamali A, Iftikhar A, Kramer LA, Papanicolaou AC, Fletcher JM, Ewing-Cobbs L. 2009. Diffusion tensor tractography quantification of the human corpus callosum fiber pathways across the lifespan. *Brain Res*. 1249: 91–100.

Head D, Buckner RL, Shimony JS, Williams LE, Akbudak E, Conturo TE, McAvoy M, Morris JC, Snyder AZ. 2004. Differential vulnerability of anterior white matter in nondemented aging with minimal acceleration in dementia of the Alzheimer type: evidence from diffusion tensor imaging. *Cereb Cortex*. 14:410–423.

Henning J. 1988. Multiecho imaging sequences with low refocusing flip angles. *J Magn Reson*. 78:397–407.

Hofer S, Frahm J. 2006. Topography of the human corpus callosum revisited–comprehensive fiber tractography using diffusion tensor magnetic resonance imaging. *NeuroImage*. 32:989–994.

Hou J, Pakkenberg B. 2012. Age-related degeneration of corpus callosum in the 90+ years measured with stereology. *Neurobiol Aging*. 33:e1001–e1009, 1009.

Jenkinson M, Beckmann CF, Behrens TE, Woolrich MW, Smith SM. 2012. Fsl. *NeuroImage*. 62:782–790.

Jones DK, Cercignani M. 2010. Twenty-five pitfalls in the analysis of diffusion MRI data. *NMR Biomed*. 23:803–820.

Jones DK, Knosche TR, Turner R. 2013. White matter integrity, fiber count, and other fallacies: the do's and don'ts of diffusion MRI. *NeuroImage*. 73:239–254.

Kaes. 1907. Die Grosshirnrinde des Menschen in ihren Massen und in ihrem Fasergehalt. In: *Ein Gehirnanatomischer Atlas Gustav Fischer; Jena*.

Kochunov P, Ganjgahi H, Winkler A, Kelly S, Shukla DK, Du X, Jahanshad N, Rowland L, Sampath H, Patel B *et al*. 2016. Heterochronicity of white matter development and aging explains regional patient control differences in schizophrenia. *Hum Brain Mapp*. 37:4673–4688.

LaMantia AS, Rakic P. 1990a. Axon overproduction and elimination in the corpus callosum of the developing rhesus monkey. *J Neurosci*. 10:2156–2175.

LaMantia AS, Rakic P. 1990b. Cytological and quantitative characteristics of four cerebral commissures in the rhesus monkey. *J Comp Neurol*. 291:520–537.

Lankford CL, Does MD. 2013. On the inherent precision of mcDESPOT. *Magn Reson Med*. 69:127–136.

Laule C, Kozlowski P, Leung E, Li DKB, MacKay AL, Moore GRW. 2008. Myelin water imaging of multiple sclerosis at 7T: correlations with histopathology. *NeuroImage*. 40:6.

Laule C, Leung E, Lis DK, Traboulsee AL, Paty DW, MacKay AL, Moore GR. 2006. Myelin water imaging in multiple sclerosis: quantitative correlations with histopathology. *Mult Scler*. 12:747–753.

Lebel C, Gee M, Camicioli R, Wieler M, Martin W, Beaulieu C. 2012. Diffusion tensor imaging of white matter tract evolution over the lifespan. *NeuroImage*. 60:340–352.

Lee MK, Cleveland DW. 1994. Neurofilament function and dysfunction: involvement in axonal growth and neuronal disease. *Curr Opin Cell Biol*. 6:34–40.

Lintl P, Braak H. 1983. Loss of intracortical myelinated fibers: a distinctive age-related alteration in the human striate area. *Acta Neuropathol*. 61:178–182.

MacKay A, Whittall K, Adler J, Li D, Paty D, Graeb D. 1994. In vivo visualization of myelin water in brain by magnetic resonance. *Magn Reson Med*. 31:673–677.

Marner L, Nyengaard JR, Tang Y, Pakkenberg B. 2003. Marked loss of myelinated nerve fibers in the human brain with age. *J Comp Neurol*. 462:144–152.

Marques JP, Kober T, Krueger G, van der Zwaag W, Van de Moortele PF, Gruetter R. 2010. MP2RAGE, a self bias-field corrected sequence for improved segmentation and T1-mapping at high field. *NeuroImage* 49:1271–1281.

Mårtensson J, Lätt J, Åhs F, Fredrikson M, Söderlund H, Schiöth HB, Kok J, Kremer B, van Westen D, Larsson EM *et al*. 2018. Diffusion tensor imaging and tractography of the white matter in normal aging: the rate-of-change differs between segments within tracts. *Magn Reson Imaging*. 45:113–119.

McCreary CR, Bjarnason TA, Skihar V, Mitchell JR, Yong VW, Dunn JF. 2009. Multiexponential T2 and magnetization transfer MRI of demyelination and remyelination in murine spinal cord. *NeuroImage*. 45:1173–1182.

Meiboom S, Gill D. 1958. Modified spin-Echo method for measuring nuclear relaxation times. *Rev Sci Instrum*. 29:688–691.

Meier-Ruge W, Ulrich J, Bruhlmann M, Meier E. 1992. Age-related white matter atrophy in the human brain. *Ann N Y Acad Sci*. 673:260–269.

Menon RS, Rusinko MS, Allen PS. 1992. Proton relaxation studies of water compartmentalization in a model neurological system. *Magn Reson Med*. 28:264–274.

Michielse S, Coupland N, Camicioli R, Carter R, Seres P, Sabino J, Malykhin N. 2010. Selective effects of aging on brain white matter microstructure: a diffusion tensor imaging tractography study. *NeuroImage*. 52:1190–1201.

Miller DJ, Duka T, Stimpson CD, Schapiro SJ, Baze WB, McArthur MJ, Fobbs AJ, Sousa AM, Sestan N, Wildman DE *et al*. 2012. Prolonged myelination in human neocortical evolution. *Proc Natl Acad Sci U S A*. 109:16480–16485.

Pandya DN, Karol EA, Heilbronn D. 1971. The topographical distribution of interhemispheric projections in the corpus callosum of the rhesus monkey. *Brain Res*. 32:31–43.

Peters A. 2002. The effects of normal aging on myelin and nerve fibers: a review. *J Neurocytol*. 31:581–593.

Peters A, Sethares C. 2002. Aging and the myelinated fibers in prefrontal cortex and corpus callosum of the monkey. *J Comp Neurol*. 442:277–291.

Prasloski T, Rauscher A, MacKay AL, Hodgson M, Vavasour IM, Laule C, Madler B. 2012. Rapid whole cerebrum myelin water imaging using a 3D GRASE sequence. *NeuroImage*. 63:533–539.

Radloff LS. 1977. The CES-D scale: a self-report depression scale for research in the general population. *Appl Psychol Meas*. 1:7.

Raz N. 2000. Aging of the brain and its impact on cognitive performance: Integration of structural and functional findings. In: Craik FIM, Salthouse TA editors. *Handbook of Aging and Cognition - II*. Mahwah, NJ: Lawrence Erlbaum Associates, Inc. p. 1–90.

Raz N, Gunning FM, Head D, Dupuis JH, McQuain J, Briggs SD, Loken WJ, Thornton AE, Acker JD. 1997. Selective aging of the human cerebral cortex observed in vivo: differential vulnerability of the prefrontal gray matter. *Cereb Cortex*. 7:268–282.

Raz N, Lindenberger U. 2011. Only time will tell: cross-sectional studies offer no solution to the age-brain-cognition triangle: comment on Salthouse (2011). *Psychol Bull*. 137:790–795.

Raz N, Lindenberger U, Rodrigue KM, Kennedy KM, Head D, Williamson A, Dahle C, Gerstorf D, Acker JD. 2005. Regional brain changes in aging healthy adults: general trends, individual differences and modifiers. *Cereb Cortex*. 15:1676–1689.

Raz N, Rodrigue KM. 2006. Differential aging of the brain: patterns, cognitive correlates and modifiers. *Neurosci Biobehav Rev*. 30:730–748.

Rittner L, Ferro Freitas P, Appenzeller S, De Alencar Lotufo R. 2014. Automatic DTI-based parcellation of the corpus callosum through the watershed transform. *Br J Biomed Eng*. 30:132–143.

Salat DH, Tuch DS, Greve DN, van der AJ, Hevelone ND, Zaleta AK, Rosen BR, Fischl B, Corkin S, Rosas HD *et al*. 2005a. Age-related alterations in white matter microstructure measured by diffusion tensor imaging. *Neurobiol Aging*. 26: 1215–1227.

Salat DH, Tuch DS, Hevelone ND, Fischl B, Corkin S, Rosas HD, Dale AM. 2005b. Age-related changes in prefrontal white matter measured by diffusion tensor imaging. *Ann N Y Acad Sci*. 1064:37–49.

Sanchez I, Hassinger L, Paskevich PA, Shine HD, Nixon RA. 1996. Oligodendroglia regulate the regional expansion of axon caliber and local accumulation of neurofilaments during development independently of myelin formation. *J Neurosci*. 16:5095–5105.

Seltzer B, Pandya DN. 1983. The distribution of posterior parietal fibers in the corpus callosum of the rhesus monkey. *Exp Brain Res*. 49:147–150.

Tang Y, Nyengaard JR, Pakkenberg B, Gundersen HJ. 1997. Age-induced white matter changes in the human brain: a stereological investigation. *Neurobiol Aging*. 18:609–615.

Vargas WS, Monohan E, Pandya S, Raj A, Vartanian T, Nguyen TD, Hurtado Rua SM, Gauthier SA. 2015. Measuring longitudinal myelin water fraction in new multiple sclerosis lesions. *Neuroimage Clin*. 9:369–375.

Webb S, Munro CA, Midha R, Stanisz GJ. 2003. Is multicomponent T2 a good measure of myelin content in peripheral nerve? *Magn Reson Med*. 49:8.

West DJ, Teixeira R, Wood TC, Hajnal JV, Tournier JD, Malik SJ. 2019. Inherent and unpredictable bias in multi-component DESPOT myelin water fraction estimation. *NeuroImage*. 195:78–88.

West RL. 1996. An application of prefrontal cortex function theory to cognitive aging. *Psychol Bull*. 120:272–292.

Westlye LT, Walhovd KB, Dale AM, Bjornerud A, Due-Tonnessen P, Engvig A, Grydeland H, Tamnes CK, Ostby Y, Fjell AM. 2010. Life-span changes of the human brain white matter: diffusion tensor imaging (DTI) and volumetry. *Cereb Cortex*. 20:2055–2068.

Whittall KP, MacKay AL, Graeb DA, Nugent RA, Li DK, Paty DW. 1997. In vivo measurement of T2 distributions and water contents in normal human brain. *Magn Reson Med*. 37:34–43.

Whittall KP, MacKay AL, Li DK, Vavasour IM, Jones CK, Paty DW. 2002. Normal-appearing white matter in multiple sclerosis has heterogeneous, diffusely prolonged T(2). *Magn Reson Med*. 47:403–408.

Yakovlev PI, Lecours AR. 1967. The myelogenetic cycles of regional maturation of the brain. In: Minkowski A, editor. *Regional Development of the Brain Early in Life*. Vol 68. Oxford, UK: Blackwell Scientific Publications Inc.

Yu Q, Daugherty AM, Anderson DM, Nishimura M, Brush D, Hardwick A, Lacey W, Raz S, Ofen N. 2018. Socioeconomic status and hippocampal volume in children and young adults. *Dev Sci*. 21:e12561.

Zhang J, Kolind SH, Laule C, MacKay AL. 2015. How does magnetization transfer influence mcDESPOT results? *Magn Reson Med*. 74:1327–1335.

Zhang Y, Brady M, Smith S. 2001. Segmentation of brain MR images through a hidden Markov random field model and the expectation-maximization algorithm. *IEEE Trans Med Imaging*. 20:45–57.